

1 **Insoluble lipid film mediates transfer of soluble saccharides from the sea to the**  
2 **atmosphere: the role of hydrogen bonding**

3 Minglan Xu, Narcisse Tsona Tchinda, Jianlong Li, Lin Du\*

4 Environment Research Institute, Shandong University, Binhai Road 72, Qingdao,  
5 266237, China

6 Correspondence: Lin Du ([lindu@sdu.edu.cn](mailto:lindu@sdu.edu.cn))

7

8 **Abstract**

9 Saccharides are a large portion of organic matter in sea spray aerosol (SSA). Although  
10 they can affect climate-related properties of SSA, the mechanism through which  
11 saccharides are transferred from bulk seawater to the ocean surface and ultimately  
12 into SSA is still debated. Here, the transfer of small soluble saccharides was validated  
13 using a controlled plunging jet sea spray aerosol generator to better understand the  
14 wide range of particle properties produced by natural seawater mixed with model  
15 organic species, glucose and trehalose. We showed that both soluble saccharides can  
16 promote the production of SSA particles, and the presence of trehalose could increase  
17 the SSA number concentration by 49.4%. Conversely, the role of the insoluble fatty  
18 acid film on the seawater surface greatly reduced the production of SSA. The  
19 resulting inorganic-organic mixed particles identified by the transmission electron  
20 microscope (TEM) showed typical core-shell morphology. Langmuir model was used  
21 to parameterize the adsorption and distribution of saccharide into SSA across the  
22 bubble surface, while infrared reflection-absorption spectroscopy (IRRAS) combined  
23 with Langmuir isotherms were undertaken to examine the effects of aqueous subphase  
24 soluble saccharides with various concentrations on the phase behavior, structure and  
25 ordering of insoluble lipid monolayers adsorbed at the air/water interface. We found  
26 that the adsorption of glucose and trehalose on the fatty acid monolayer led to the  
27 expansion of the mean molecular area. Saccharide-lipid interactions increased with  
28 increasing complexity of the saccharide in the order glucose < trehalose. On seawater  
29 solution, the effects of dissolved saccharides on the ordering and organization of fatty

30 acid chains were muted. The enhancement of the carbonyl band to the low  
31 wavenumber region implied that soluble saccharides can form new hydrogen bonds  
32 with fatty acid molecules by displacing large amounts of water near the polar head  
33 groups of fatty acids. Our results indicate that the interaction between soluble  
34 saccharides and insoluble fatty acid molecules through hydrogen bonds is an  
35 important component of the sea-air transfer mechanism of saccharides.

## 36 **1 Introduction**

37 Sea spray aerosol (SSA) represents a major source of aerosol particle populations  
38 and significantly impacts the earth's radiation budget, cloud formation and  
39 microphysics by serving as cloud condensation nuclei (CCN) and ice nuclei (IN), and  
40 microbial cycling (Bertram et al., 2018; Partanen et al., 2014). The formation of SSA  
41 particles is strongly influenced by the uppermost sea surface microlayer (SML),  
42 which is a thin layer of 1–1000  $\mu\text{m}$  thickness formed due to different physicochemical  
43 properties of air and seawater (Wurl et al., 2017). Beyond sea salt, the ocean surface  
44 contains a fair amount of organic matter (OM) mass fraction, covering carbohydrates,  
45 lipids, proteins, humic-like substances (HULIS), intact phytoplankton cells and  
46 fragments, fungi, viruses, and bacteria (Van Pinxteren et al., 2020; Cunliffe et al.,  
47 2013). These organic matter coincides with some chemical markers that is enriched in  
48 the SSA, which is mainly produced by bubble-mediated (Russell et al., 2010; Facchini  
49 et al., 2008). When a bubble reaches the water surface, destroying the surface  
50 membrane of the water, the bubble bursts into many so-called film drops. After the

51 bubble film breaks, a jet of water rising vertically from the ruptured bubble cavity  
52 forms so-called jet drops. Film drops are responsible for the major proportion  
53 (~60%–80%) of submicron particles, whereas jet drops contribute significantly to the  
54 production of supermicron particles (Wang et al., 2017). Both the size and chemical  
55 composition of SSA are important properties in determining cloud formation and  
56 eventually radiative forcing (Brooks and Thornton, 2018). Hence, understanding the  
57 physico-chemical mechanisms driving these variations is essential for predicting SSA  
58 composition and climate-related processes.

59 Surface-active biomolecules are preferentially transferred from marine surface  
60 water into the atmosphere through the bubble bursting processes, forming a  
61 considerable fraction of primary marine organic aerosols (Schmitt-Kopplin et al.,  
62 2012). Previous measurements have shown that up to 60% of ocean particle mass can  
63 be organic, which exhibits a strong size dependence (O'dowd et al., 2004; Russell et  
64 al., 2010). Spectroscopic evidence from field-collected SSA particles indicates that  
65 the oxygen-rich organic fractions of individual particles contain molecular signatures  
66 of saccharides and carboxylic acids (Hawkins and Russell, 2010). For example, it has  
67 previously been observed that the carbohydrate-like spectroscopic signatures account  
68 for 40–61% of the submicron SSA organic mass (Quinn et al., 2014; Russell et al.,  
69 2010). A large portion of this mass is attributed to saccharides that are transferred  
70 from seawater to SSA, and shows a certain enrichment in SSA. Specifically, the high  
71 enrichment factor of carbohydrates was calculated for supermicron (20–4000) and  
72 submicron (40–167000) particles relative to the bulk seawater in the Western

73 Antarctic Peninsula (Zeppenfeld et al., 2021). According to previous laboratory  
74 studies, marine bacteria, divalent cations and protein can affect the saccharide  
75 enrichment in SSA (Hasenecz et al., 2020; Schill et al., 2018). However, a  
76 mechanistic and predictable understanding of these complex and interacting processes  
77 in favor of saccharides found in marine aerosol particles remains largely unexplored,  
78 despite their oceanic and atmospheric significance.

79 A variety of saccharides have been found ubiquitous in the ocean, including  
80 dissolved free monosaccharides, oligo/polysaccharides, sugar alcohols, and  
81 monosaccharide dehydrates, the composition of which depends on marine biological  
82 activity (Van Pinxteren et al., 2012). Frossard et al. (2014) used the hydroxyl  
83 characteristic functional group of atmospheric marine aerosols from Fourier transform  
84 infrared spectroscopy to infer the contributions of different saccharides in SSA. It was  
85 found that the primary marine aerosols produced in biologically productive seawater  
86 had stronger hydroxyl group characteristic of monosaccharides and disaccharides,  
87 while the hydroxyl groups of seawater organic matter were closer to those of  
88 polysaccharides. This suggests that larger saccharides may be preferentially retained  
89 in seawater during aerosol production. Analysis of aerosol samples collected on the  
90 Western Antarctic Peninsula also showed that not only polysaccharides but also a high  
91 portion of free monosaccharides mainly composed of glucose, fructose, rhamnose and  
92 glucosamine were present (Zeppenfeld et al., 2021). Raman spectroscopy was used to  
93 measure individual SSA particles generated via wave breaking in a wave flume under  
94 algal bloom conditions to get a deeper insight into their organic categories. It was

95 reported that 4%–17% and 3%–46% of sub- and supermicron particles show strong  
96 spectral characteristics of free saccharides and short-chain fatty acids, respectively  
97 (Cochran et al., 2017). However, current climate models largely underestimate the  
98 ratio of saccharides in marine aerosols (Cravigan et al., 2020), and there is an urgent  
99 need to clarify the physicochemical mechanisms that drive saccharides transfer to  
100 SSA.

101 A possible explanation for the origin of saccharides in SSA chemical composition  
102 involves the affinity between the bulk aqueous soluble saccharides and insoluble  
103 surfactant monolayers already adsorbed at the air/water interface, resulting in  
104 co-adsorption of the soluble saccharides (Link et al., 2019b). This co-adsorption arises  
105 from non-covalent interactions and promotes the binding of soluble organic matter to  
106 the surface with insoluble Langmuir film. Previous studies have indicated that the  
107 presence of lipids or proteins strongly enhances the surface adsorption capacity of  
108 saccharides, even for highly soluble saccharides that do not adsorb individually at the  
109 air/water interface (Pavinatto et al., 2007; Burrows et al., 2016). For example, recent  
110 studies have shown that simple, soluble biomolecules such as phenylalanine and  
111 trehalose exhibit an affinity for lipid films, altering membrane permeability and phase  
112 behavior (Perkins and Vaida, 2017; Link et al., 2019a). A divalent cation-mediated  
113 co-adsorption mechanism was also proposed to explain the enrichment of  
114 monosaccharide in laboratory-generated SSA (Schill et al., 2018). Alternatively,  
115 saccharides can be bound covalently to larger, more surface-active biomolecules, such  
116 as glycoproteins or lipopolysaccharides, which attach to SML and are eventually

117 transferred into SSA through bubble bursting at the ocean surface (Estillore et al.,  
118 2017). Although different hypotheses have been proposed, there is still debate about  
119 the more nuanced mechanisms that guide the sugar-lipid interactions in the marine  
120 environment.

121 The present work aims to use a multipronged approach that combines bulk SSA  
122 production experiments, Langmuir surface pressure-area isotherms and infrared  
123 reflection-absorption spectroscopy (IRRAS) to examine the role of saccharides in  
124 SSA production and the mechanism of saccharides transfer and enrichment from  
125 aqueous solution into SSA. The study focuses on two soluble saccharides that are  
126 prevalent in seawater, glucose and trehalose, which are uncharged monosaccharide  
127 and disaccharide, respectively. A plunging jet sea spray aerosol generator was used to  
128 generate nascent SSA particles by artificially generating bubbles in seawater as a  
129 mean of simulating sea spray production by breaking waves. This simulation helps  
130 evaluate the impact of soluble saccharides as well as insoluble fatty acids on SSA  
131 production and particle morphology. Langmuir isotherms provided abundant  
132 information for stability and fluidity of monolayers, which were used to adequately  
133 describe the magnitude of interaction effects between subphase soluble saccharides  
134 and surface insoluble surfactants. Finally, IRRAS spectra provided molecular scale  
135 descriptions of monolayer conformational information and allowed us to deduce the  
136 distribution of saccharide species at the interface. By combining all the findings, we  
137 propose a model of sea-air transfer of marine saccharides through hydrogen bond  
138 interactions involved in surface insoluble lipid molecules.

## 139 **2 Experimental sections**

### 140 **2.1 Materials and solutions**

141 D-(+)-Glucose (Glu, powder,  $\geq 99.5\%$ ) and D-(+)-Trehalose anhydrous (Tre, powder,  
142 99%) were purchased from Aladdin. Stearic acid (SA,  $>98\%$ , TCI), palmitic acid  
143 (PA,  $>98\%$ , Adamas-beta) and myristic acid (MA,  $\geq 99.5\%$ , Aladdin) were prepared in  
144 chloroform (AR,  $\geq 99.0\%$ , Sinopharm Chemical Reagent Co., Ltd) at a final  
145 concentration of 1 mM each. Figure S1 shows the chemical structures of the three  
146 fatty acids used in this study. The respective fatty acid solutions were mixed at a  
147 molar ratio of 2 MA:4 PA:3 SA to obtain a mixed lipid stock solution considering that  
148 PA and SA account for approximately two-thirds of the total saturated fatty acids in  
149 fine SSA particles, with MA being the third most abundant species (Cochran et al.,  
150 2016). All chemicals were used without further purification. The natural seawater  
151 (SW) was collected from Shazikou, Qingdao, China. Here, surface seawater (within  
152 0.1~1 m below the sea surface) was obtained from a pier on the coast by immersing  
153 high-density polyethylene containers into the water. The sampled seawater was  
154 microfiltered through 0.2  $\mu\text{m}$  polyethersulfone filter (Supor<sup>®</sup>-200, Pall Life Sciences,  
155 USA) to remove large particles such as sediments, algae and bacteria. The filtered  
156 seawater was used for SSA generation and as a filling subphase for interfacial  
157 experiments. The pH of natural seawater, initially determined to be about  $8.13 \pm 0.02$ ,  
158 was measured to be around  $8.04 \pm 0.01$  at the end of the experiment. Different  
159 concentrations of saccharide-containing seawater solutions required in the

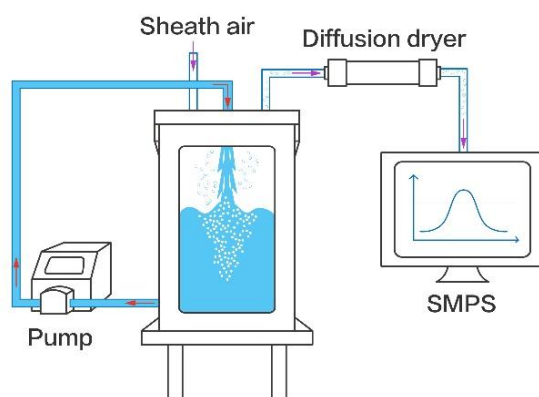


160 experiments were obtained by dissolving different masses of glucose or trehalose in  
161 the filtered natural seawater using mechanical stirring.

## 162 **2.2 SSA production and collection**

163 SSAs were produced using a plunging jet-sea spray aerosol generator (Figure 1). A  
164 physical drawing of the aerosol generation system can be found in Figure S2. The  
165 generator and its detailed operation principle has been described elsewhere (Liu et al.,  
166 2022). Briefly, the generator consists of a stainless steel (shipboard class, 316L)  
167 rectangular sealed container and a viewable glass window. The upper removable lid  
168 has ports for water inlet, purging air, and sampling. The purge air is supplied by a  
169 zero-air generator (Model 111, Thermo Scientific, USA) and the flow rate is  
170 controlled at 10 L min<sup>-1</sup>. A peristaltic pump (WL600-1A, ShenChen) periodically  
171 circulates water from the bottom of the generator to the top nozzle through a Teflon  
172 tube with a pump speed of 1 L min<sup>-1</sup>, creating a plunging water column that hits the  
173 seawater surface and entrains air into the bulk seawater. The bubble plumes extend  
174 approximately 15 cm down into the water, a moderate depth considering that the  
175 majority of the air being entrained in is located within about 50 cm from the sea  
176 surface (Hultin et al., 2010). When the bubbles rise to the air/water interface and burst,  
177 they generate SSA emissions. When studying insoluble surfactant effects, a  
178 concentrated solution of 1 mM mixed fatty acids in chloroform was added to the  
179 surface of the seawater solution. After the necessary fatty acids were added, only the  
180 sheath air flowed, allowing the chloroform to evaporate for 15 min and leaving only

181 the surfactant on the surface. After pre-preparation for 15 min, the sheath air and  
182 peristaltic pump were turned on to produce SSAs. Prior to collection, SSAs were  
183 dried to a relative humidity of ~40% using a diffusion dryer. Thereafter, a scanning  
184 mobility particle sizer (SMPS, model 3936, TSI) consisting of a differential mobility  
185 analyzer (DMA, model 3081, TSI Inc., USA) and a condensation particle counter  
186 (CPC, model 3776, TSI Inc., USA) was used to measure the particle size distributions  
187 and number concentrations. The particle size distribution ranging from 13.6 to 710.5  
188 nm was obtained at a sheath flow rate of 3.0 L min<sup>-1</sup> and aerosol flow rate of 0.3 L  
189 min<sup>-1</sup>. Dried SSAs were deposited onto 200 mesh copper grids with carbon foil  
190 (T11023, Tilan, China) by a single particle sampler (DKL-2, Genstar electronic  
191 technology Co., Ltd) to further characterize the particle morphology.



192  
193 Figure 1. Schematic picture of the plunging jet-sea spray aerosol generator. The red  
194 arrows represent the flow direction of seawater, and the purple arrows represent the  
195 flow of gases and aerosols.

### 196 **2.3 Langmuir monolayer preparation and Langmuir isotherms**

197 The Langmuir trough setup has been described previously (Xu et al., 2021). Briefly, it  
198 consists of a rectangular Teflon trough (Riegler & Kirstein, Germany) and two  
199 moveable Teflon barriers whose movements are precisely controlled to achieve  
200 symmetric compression of the monolayer at the air/water interface. A Wilhelmy plate  
201 attached to the pressure sensor was used to measure the surface pressure. Each 100  
202 mL subphase consisted of natural seawater, with varying amounts of glucose or  
203 trehalose. Aliquots of mixed fatty acids stock solution were spread onto the subphase  
204 surface dropwise with a glass microsyringe and 15–20 min were allowed for solvent  
205 evaporate completely. The surface pressure ( $\pi$ ), given by eq 1 and defined as the  
206 difference in surface tension between the pure air/water interface ( $\gamma_0$ ) and the  
207 monolayer covered interface ( $\gamma$ ) was monitored.

$$208 \quad \pi = \gamma_0 - \gamma \quad (1)$$

209 The barriers were compressed at a rate of 3 mm min<sup>-1</sup> per barrier and isotherm data  
210 were collected for surface pressure  $\pi$  (mN m<sup>-1</sup>) versus area per molecule (Å<sup>2</sup>). All  
211 experiments were performed at (22 ± 3) °C and relative humidity below 65%.

### 212 **2.4 Infrared reflection-absorption spectroscopy measurement**

213 The polarization-modulation infrared reflection-absorption spectroscopy (PM-IRRAS)  
214 is a mainstream spectroscopic method for in-situ characterization of Langmuir  
215 monolayers at the molecular level. For IRRAS spectra, floating monolayers were  
216 spread at the aqueous subphase and compressed to the desired surface pressure, and

217 stopped before obtaining the spectra. PM-IRRAS spectra were obtained using a  
218 Fourier transform infrared (FT-IR) spectrometer (Bruker Vertex 70, Germany)  
219 equipped with an external reflection accessory (XA-511). The interference infrared  
220 beam was set out from FT-IR and polarized by a ZnSe polarizer to alternately  
221 generate s- and p-polarization lights. They were then continuously modulated by a  
222 photoelastic modulator (PEM-100) at a high frequency of 42 kHz to measure the  
223 spectra of both polarizations simultaneously. The infrared beam was focused onto the  
224 Langmuir film through a gold mirror, and then a portion of reflected light was  
225 directed onto the liquid nitrogen-cooled mercury-cadmium-telluride (MCT) detector.  
226 The application of polarization modulation attenuates the noise of reflective FT-IR  
227 and the interference of water vapor and carbon dioxide. The spectra presented here are  
228 reflectance-absorbance ( $RA$ ) given as:

$$229 \quad RA = -\log(R/R_0) \quad (2)$$

230 where  $R$  and  $R_0$  are the reflectance of fatty acid monolayer and pure seawater solution  
231 surface, respectively. To obtain a better signal-to-noise ratio, spectra were collected  
232 with 2000 scans and  $8 \text{ cm}^{-1}$  resolution at a fixed incidence angle of  $40^\circ$ . To better  
233 compare the variation in the spectral region of interest, peaks were fitted to Gaussian  
234 functions using Origin 2021 for each displayed spectrum.

## 235 **2.5 Transmission electron microscope imaging**

236 Particle imaging was performed using a transmission electron microscope (TEM, FEI  
237 Tecnai G2 F20, FEI, USA) equipped with a Schottky field emission gun. It was

238 operated at an accelerated voltage of 20–200 kV with a high angle annular dark field  
239 detector to collect TEM images and even preserve the soft internal structure of  
240 organic sources under high vacuum conditions.

## 241 **3 Results and discussion**

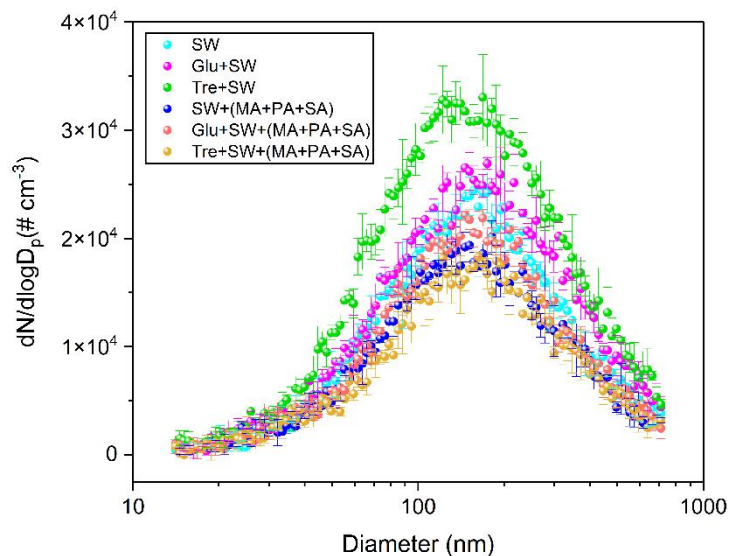
### 242 **3.1 SSA particle number size distributions**

243 To examine the sea-air transfer of soluble saccharides and their interaction with  
244 insoluble fatty acids, SSA particle generation experiments were carried out with  
245 seawater containing 1.0 g L<sup>-1</sup> glucose or trehalose. Figure 2 shows the particle number  
246 size distributions resulting from seawater to which different soluble saccharides were  
247 added in the presence or absence of fatty acids on the surface. As a reference, the  
248 particle size distribution produced from natural seawater is also given. The submicron  
249 particle size distributions produced by the plunging jet generator are well represented  
250 by lognormal mode. In the absence of saccharide, a broad, unimodal mode of the  
251 particle size distribution around 168 nm was generated. This observation agrees quite  
252 well with a previous study that produced SSA by the plunging jet method with the  
253 mode of the particle size distribution ~162 nm (Christiansen et al., 2019). Moreover,  
254 the SSA yielded by plunging waterfall also has a size distribution similar to that  
255 yielded by the breaking wave, which particle number size distribution is ~162 nm  
256 (Prather et al., 2013). This contrasts with most previous laboratory studies using  
257 sintered glass filters or frits, which tend to exhibit a smaller mean diameter and  
258 narrower distribution. This may be expected, given that similar bubble size

259 distributions exist in the two generation mechanisms using plunging waterfall and  
260 breaking waves. A previous study using plunging jets has produced similar bubble  
261 size distributions (Fuentes et al., 2010). Importantly, the measured bubble spectrum  
262 for the breaking waves matches the shape and Hinze scale of the bubble spectra of the  
263 previously measured open ocean breaking waves (Deane and Stokes, 2002). Although  
264 we did not directly measure the bubble spectra generated by the plunging jet method  
265 in this study, it should be able to better simulate the properties of breaking waves  
266 according to the above empirical studies. Moreover, we compared the particle size  
267 distributions of SSA generated in our laboratory with those measured in field studies  
268 (Quinn et al., 2017; Xu et al., 2022). As shown in Figure S3, it was observed that the  
269 size distribution of both laboratory-generated SSAs and SSAs measured in the field  
270 had a major accumulation mode in the range of ~111–172 nm. However, the number  
271 concentration of SSAs produced in our experiment is about 2 orders of magnitude  
272 higher than that in the real environment. As a result, the jet sea spray generator system  
273 is capable of a wide range of measurements (e.g., size-resolved hygroscopicity and  
274 heterogeneous reactivity) that are not achievable at low number concentrations.

275 Laboratory studies of the effects of saccharide organic substances on droplet  
276 production have been inconclusive. A previous study has used two bubble generation  
277 methods (plunging water jet and diffusion aeration) to investigate the number size  
278 distribution of SSA particles produced by mixing fructose and mannose with NaCl or  
279 artificial seawater solution (King et al., 2012). The results showed that the number  
280 concentration of particles produced by artificial seawater containing sodium dodecyl

281 sulfate was significantly lower than that of particles produced by artificial seawater  
282 containing fructose. However, NaCl solution containing mannose produced SSA with  
283 lower number concentration than NaCl solution containing sodium laurate. Lv et al.  
284 (2020) found that addition fructose to sea salt solution can significantly promote the  
285 increase of SSA number concentration. However, the above studies lacked direct  
286 comparative results on SSA production influenced by different soluble saccharides.  
287 For the plunging jet, our measurements indicate that soluble saccharides can promote  
288 the production of SSA to varying degrees. The number concentration, mass  
289 concentration, and geometric mean diameter are shown in supplement Table S1 for  
290 further details. It was observed that glucose led to a slight increase of about 15.6% in  
291 particle number concentration, increasing the mode diameters to ~175 nm. In contrast,  
292 the natural seawater spiked with trehalose resulted in a higher total particle number  
293 concentration that increased by approximately 49.4% over a wide size range.  
294 Therefore, the changes in production and properties of SSA from actual seawater may  
295 be more complicated under the influence of different saccharides.



296

297 Figure 2. The particle number size distribution spectra of SSAs produced from blank  
 298 seawater sample and seawater sample spiked with glucose or trehalose. Both results  
 299 are presented here with and without fatty acid surface films.

300 The effect of the interaction of insoluble fatty acids with different saccharides on  
 301 SSA particles was investigated by spreading insoluble fatty acids on seawater surface.  
 302 In plain sight, fatty acids on the surface can significantly reduce the number  
 303 concentration of SSA regardless of the presence of saccharides in the seawater. When  
 304 the fatty acid surfactant was added to seawater alone, the number concentration  
 305 decreased by about 17.2%, while the presence of glucose resulted in a decrease of  
 306 about 21.6%. Moreover, fatty acids showed the highest inhibitory effect on SSA  
 307 produced by trehalose-containing seawater solution, whose concentration decreased  
 308 by about 49.4%. We ascribe that the surface layer is significantly more stable in the  
 309 presence of fatty acids, even when disturbed by the plunging jet, thus resulting in less  
 310 bubble bursting. Furthermore, the continuous plunging caused a layer of foam to  
 311 accumulate on the surface of the water. The presence of the foam layer on the



312 seawater surface may be capable of prohibiting the production of droplets by  
313 assimilating rising bubbles into the foam layer before bursting. Collectively, the  
314 observed variability in these experiments suggests an urgent need to better build the  
315 link between total SSA particle flux and seawater organic composition over the ocean.  
316 However, sole bulk-phase generation experiments may not accurately capture the  
317 relevant chemical behaviors and support mechanism analysis that occur in the SML.  
318 Therefore, we attempted to explore the possible interaction mechanisms via air/water  
319 interface chemical experiments.

### 320 **3.2 $\pi$ -A isotherms of fatty acid monolayers**

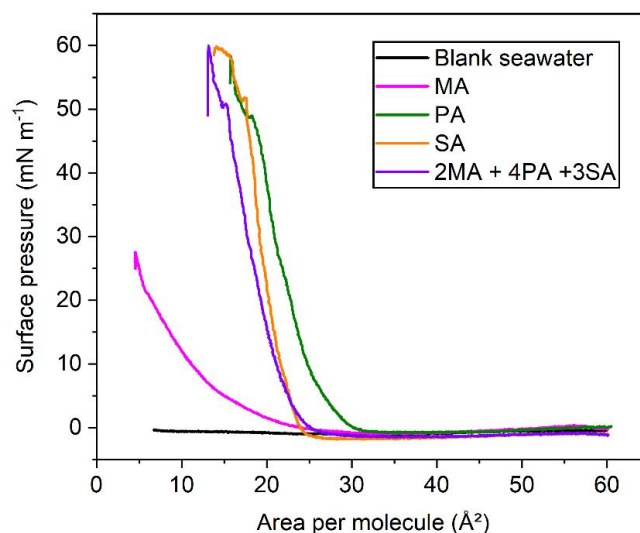
321 In this section, we only discuss traditional Langmuir monolayers, which operate on  
322 air/water interfaces that are ubiquitous along the sea surface (Elliott et al., 2014). The  
323  $\pi$ -A isotherm reflects information on the phase behavior of the monolayer as a  
324 function of lipid packing density. As shown in Figure 3, the  $\pi$ -A isotherms of  
325 individual and mixed fatty acids on the natural seawater subphase are presented.  
326 When the mechanical barriers initially begin to compress, the amphiphilic molecules  
327 in the monolayer are in the gaseous (G) phase under a large area per molecule, with  
328 the hydrophobic tails having significant contact with the water surface, but little  
329 contact with each other. At this stage, the compression of the film does not lead to a  
330 significant change in surface pressure. As the monolayer is compressed, the  
331 intermolecular distances gradually decrease and the surface pressure begins to rise  
332 from zero into the liquid expanded (LE) phase, where the hydrophobic tails start to

333 touch each other, but remain largely disordered and fluid. This is represented as the  
334 lift-off area of the isotherm. Further compression results in a thermodynamic  
335 transition to a liquid condensed (LC) phase. The film is eventually compressed to a  
336 limiting point where the monolayer collapses as the materials leave the 2D film (Lee,  
337 2008). In general, the collapse is an irreversible process, and the collapsed material  
338 does not reintegrate into the monolayer as the surface pressure decreases.

339 Although the  $\pi$ -A isotherms of individual fatty acids have been well studied, the  
340 phase behavior of the mixed binary and ternary systems still needs to be further  
341 explored. Pure natural seawater without spreading surface-active fatty acids does not  
342 cause observable changes in the surface pressure, indicating that surface-active  
343 impurities are either absent or have too low concentrations to cause film formation.  
344 When myristic acid spreads on the water surface, it undergoes a long liquid phase,  
345 with a lower collapse pressure of  $\sim 27 \text{ mN m}^{-1}$  and area per molecule as low as  $5 \text{ \AA}^2$ .  
346 This is due to the relatively high solubility of MA molecules in the aqueous phase,  
347 resulting in a large loss of molecules in the monolayer under the mechanical forcing  
348 from lateral barriers compression. In addition, according to the surface pKa value of  
349 7.88 at  $20 \text{ }^\circ\text{C}$ , MA is mostly deprotonated at pH  $\sim 8.1$ , so a stable monolayer cannot be  
350 obtained for the natural seawater subphase due to the dissolution phenomenon  
351 (Carter-Fenk and Allen, 2018). For palmitic acid monolayer, it goes through a  
352 relatively short gaseous phase and rapidly enters the liquid phase. After experiencing  
353 a kink point at  $\sim 48 \text{ mN m}^{-1}$ , it continues to rise to the maximum surface pressure of  
354  $\sim 57 \text{ mN m}^{-1}$  and collapses. Both the lift-off area and molecular area of the stearic acid

355 film decreased more than those of palmitic acid film. This is caused by the fact that  
356 the interaction (van der Waals force) between the molecules increases as the  
357 molecular weight of long chain fatty acid increases. That is, increased attraction leads  
358 to a decrease in distance between SA molecules.

359 When fatty acids are mixed in a certain molar ratio and spread onto the interface  
360 water, it is found that the  $\pi$ -A isotherm lies between the pure fatty acids and is closer  
361 to that of stearic acid, but the mean molecular area is relatively smaller. The partial  
362 dissolution of myristic acid most likely accounts for the smaller mean molecular area  
363 observed in the proxy mixture isotherm compared to the palmitic acid and stearic acid  
364 isotherms. Moreover, we found that the  $\pi$ -A isotherms of mixed fatty acids exhibit  
365 similar collapsing behavior to those of stearic acid and palmitic acid at a surface  
366 pressure of about  $50 \text{ mN m}^{-1}$ . Consequently, the longer fatty acids will dominate the  
367 lateral interactions of the SSA membrane, which makes the membrane more rigid due  
368 to the larger sum of diffusive interactions. In view of the true proportion of fatty acids  
369 in the nascent sea spray particles, we used a ternary fatty acid membrane proxy  
370 system composed of MA, PA, and SA (2:4:3 molar ratio) in the following experiments  
371 involving Langmuir isotherms.



372

373 Figure 3.  $\pi$ -A isotherms of myristic acid, palmitic acid, stearic acid and mixed fatty  
 374 acids. The black trace represents the background natural seawater solution with no  
 375 fatty acid spread.

### 376 3.3 Effect of soluble saccharides on the phase behavior of mixed monolayers

377 An effective way to test whether soluble saccharides associate with lipid membranes  
 378 is to examine the effect of these saccharides on the phase behavior of lipid films. The  
 379  $\pi$ - A isotherms provide insights into the overall monolayer structure, intermolecular  
 380 interactions, and the adsorption of glucose and trehalose. Both glucose and trehalose  
 381 are highly soluble ( $>1.0 \text{ g L}^{-1}$ ) in water. However, this solubility does not preclude  
 382 their presence on the surface. According to some previous studies, the dissolved  
 383 organic carbon concentration is about  $0.7\text{--}1.0 \text{ mg carbon L}^{-1}$  (Quinn et al., 2015;  
 384 Hasencz et al., 2019). Considering that saccharides in the ocean represent  
 385 approximately 20% of the dissolved organic carbon (Pakulski and Benner, 1992;  
 386 Hasencz et al., 2019), the saccharide concentration is about  $0.14\text{--}0.20 \text{ mg L}^{-1}$ . The  
 387 glucose and trehalose concentrations used for the  $\pi$ -A isotherms are approximately

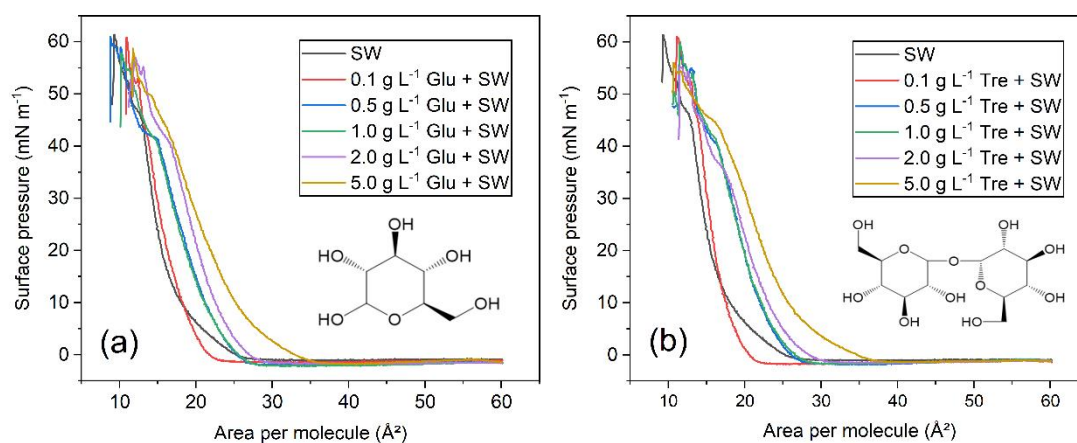
388 3–4 orders of magnitude greater than the saccharide concentration in dissolved  
389 organic matter, maintaining detectivity within the  $\pi$ -A isotherms. Furthermore, high  
390 concentrations used here are still relevant, considering the evaporation process in aged  
391 sea spray aerosols (Hasenecz et al., 2020). At the same time, such concentrations are  
392 close enough to understand the enrichment of saccharides in sea surface microlayer  
393 and to provide a confident interpretation of the physicochemical mechanisms driving  
394 the adsorption and transfer of soluble saccharides (De Vasquez et al., 2022).

395 Figure 4 shows the  $\pi$ -A isotherms of mixed fatty acids on natural seawater  
396 subphases containing different concentrations (varied between 0.1 and 5.0 g L<sup>-1</sup>) of  
397 glucose or trehalose. In this case, the surface pressure and mean molecular area of the  
398 fatty acid monolayer is equal to that of the fatty acid monolayer with the addition of  
399 saccharides, provided that the saccharide molecules do not affect the monolayer. At a  
400 low concentration of 0.1 g L<sup>-1</sup>, both saccharides had little overall effect on the phase  
401 behavior of fatty acid monolayers. However, they resulted in a smaller lift-off area for  
402 the monolayer compared to pure natural seawater. As the glucose and trehalose  
403 subphase concentration increases, the monolayers are expanded, taking up a larger  
404 mean molecular area, which is consistent with previous research (Crowe et al., 1984).  
405 This noticeable expansion can be observed from the lift-off area to collapse,  
406 indicating that saccharides participate in and disrupt the monolayer structure, and  
407 implying a degree of complexity and heterogeneous distribution of species in the  
408 interfacial region. De Vasquez et al. (2022) also demonstrated that glucuronate  
409 interacts with and expands the stearic acid monolayer. Furthermore, they suggested

410 that glucuronate intercalates into the stearic acid monolayer and leads to monolayer  
411 reorganization. Spectral evidence is needed to further clarify whether intercalation  
412 occurs in our study.

413 More surprisingly, we observed that the isotherms of the two saccharide matrices  
414 do not exhibit much difference at the concentrations of 0.5 g L<sup>-1</sup> and 1.0 g L<sup>-1</sup>. When  
415 the saccharide concentration keeps increasing to 5.0 g L<sup>-1</sup>, the molecular packing  
416 density on the interface decreases, and the apparent molecular area increases. In the  
417 presence of glucose and trehalose, the lift-off areas increased by 9 and 10 Å<sup>2</sup>,  
418 respectively. Another distinguishing feature of the fatty acid isotherms is the change  
419 of slope above ~40 mN m<sup>-1</sup>. This result could be interpreted as the saccharide being  
420 “squeezed” out of the insoluble film, resulting in higher monolayer compressibility.  
421 By squeezing saccharide molecules out of the monolayer, the isotherms at high  
422 surface pressure behave similarly to other isotherms with low saccharide  
423 concentrations. The difference is that with the increase of structural complexity of  
424 saccharide, the effect of trehalose at the same concentration is more prominent. The α,  
425 α, 1,1-linkage between two glucose subunits in trehalose is considered to provide an  
426 elastic and rigid balance, thus allowing for strong interactions with multiple fatty  
427 acids (Clark et al., 2015). As a result, trehalose binds more readily to lipid monolayer  
428 surfaces than glucose, as is evident from experimental observations. This is consistent  
429 with the result of Crowe et al. on the effect of saccharides (glucose and trehalose) on  
430 the properties of 1,2-dimyristoyl-*sn*-glycero-3-phosphocholine (DMPC) and  
431 1,2-dipalmitoyl-*sn*-glycero-3-phosphocholine (DPPC) monolayers. That is, the area

432 per lipid increases with the increase of saccharide concentration, and trehalose  
 433 provides the largest lateral monolayer expansion (Crowe et al., 1984). The expansion  
 434 effect promoted by soluble saccharides is more relevant at lower surface pressure  
 435 when alkyl chains are farther apart from each other. Clarifying and refining the  
 436 interaction mechanisms by which lipid molecules interact with saccharides is critical  
 437 to any attempt to model such chemical phenomena occurring at environmentally  
 438 relevant interfaces.



439  
 440 Figure 4.  $\pi$ -A isotherms of mixed fatty acids in the SW subphase with several  
 441 concentration gradients of (a) glucose, and (b) trehalose. The inset shows the  
 442 molecular structures of glucose and trehalose.

#### 443 3.4 Effect of soluble saccharides on the interfacial structure of mixed monolayers

444 PM-IRRAS is a surface sensitive technique that allows further study of the possible  
 445 effects of soluble saccharides on lipid interfacial organization at the molecular level.

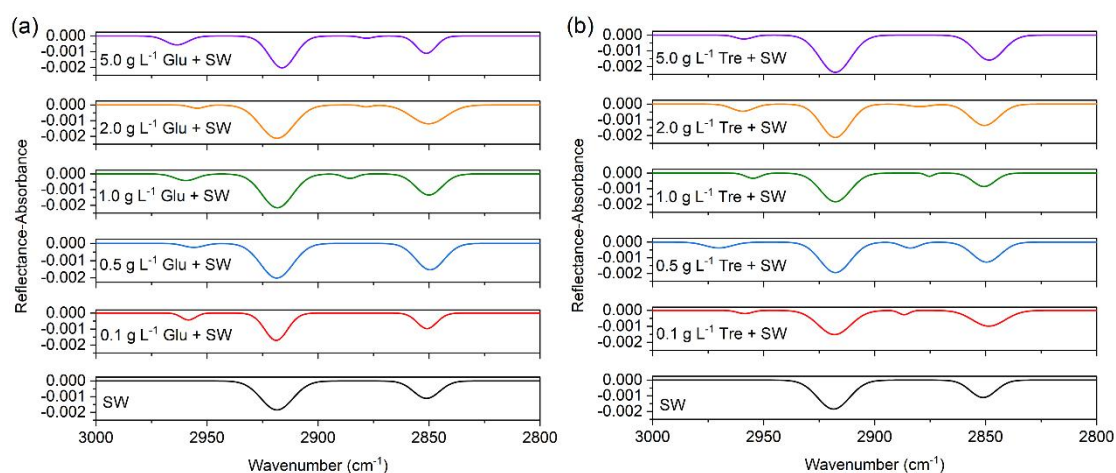
446 Figure 5 shows the IRRAS spectra for mixed fatty acid monolayers at two different  
 447 saccharides containing subphases at a surface pressure of  $\sim 30$  mN m<sup>-1</sup> to ensure  
 448 complete monolayer formation. Figure S4 shows the IRRAS spectra of mixed fatty

449 acids measured at different surface pressures. It can be observed that with the increase  
450 of surface pressure, the intensity of the peaks also increases accordingly, reaching a  
451 relatively stable level around 30 mN m<sup>-1</sup>. Considering the stability of the monolayer,  
452 this surface pressure was chosen to obtain the desired infrared spectra.

453 The absorption band in the 3000–2800 cm<sup>-1</sup> region shown in Figure 5 is ascribed to  
454 the CH stretching vibration of the alkyl chain. The main features at ~2916 and ~2850  
455 cm<sup>-1</sup> are related to antisymmetric ( $\nu_{\text{as}}(\text{CH}_2)$ ) and symmetric ( $\nu_{\text{s}}(\text{CH}_2)$ ) stretching  
456 modes of methylene of mixed fatty acids, respectively. The  $\nu_{\text{as}}(\text{CH}_2)$  feature  
457 consistently remains stronger than  $\nu_{\text{s}}(\text{CH}_2)$  with the increase of glucose and trehalose  
458 concentrations. These two band positions are often used to be empirically correlated  
459 with the order and organization within the alkyl monolayer adsorbed to the water  
460 interface, with higher wavenumbers corresponding to disordered *gauche* conformers.  
461 Conversely, low wavenumbers indicate that the alkyl chain of lipids is well ordered  
462 with preferential *all-trans* characteristics. Additionally, we also showed the  
463 wavenumbers, reflectance-absorbance intensities, peak areas and full width at half  
464 maximum (FWHM, cm<sup>-1</sup>) values of each fitted peak in Table S2 in the supplement. In  
465 this work, the relatively low frequencies of  $\nu_{\text{as}}(\text{CH}_2)$  (2916–2918 cm<sup>-1</sup>) and  $\nu_{\text{s}}(\text{CH}_2)$   
466 (2848–2851 cm<sup>-1</sup>) hint that the molecular conformation of the fatty acid alkyl chains  
467 is dominated by the highly ordered *all-trans* conformation (Li et al., 2019). Despite  
468 the concentration range of saccharides varied widely, the positions of  $\nu_{\text{as}}(\text{CH}_2)$  and  
469  $\nu_{\text{s}}(\text{CH}_2)$  showed modest sensitivity to shift, suggesting very minor changes in the  
470 conformation of the alkyl chain. The relative weak antisymmetric ( $\nu_{\text{as}}(\text{CH}_3)$ ) and



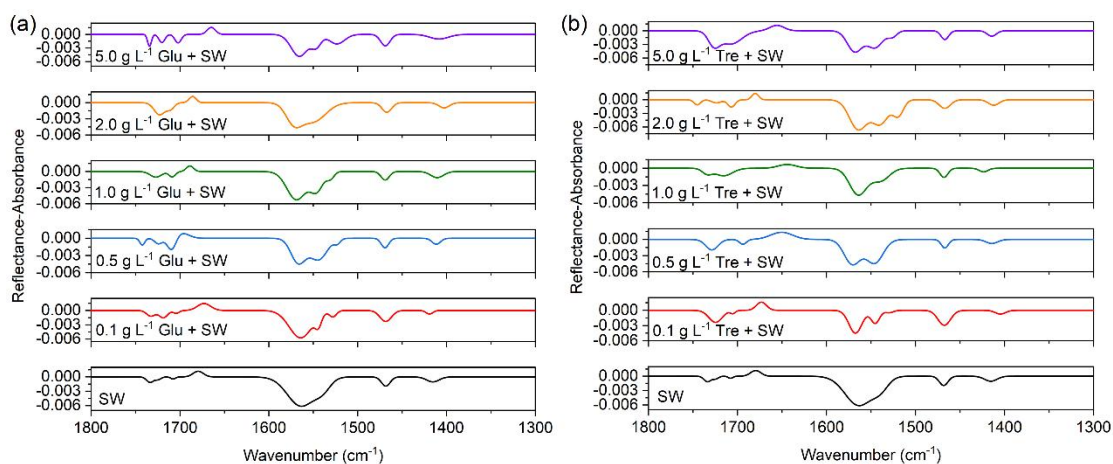
471 symmetric methyl stretching ( $\nu_s(\text{CH}_3)$ ) vibrations were observed at  $\sim 2958$  and  $\sim 2880$   
 472  $\text{cm}^{-1}$ , respectively. These results indicate that the penetration of soluble saccharides is  
 473 only superficial (along the lipid surface) and has little effect on the alkyl tail  
 474 arrangement. Therefore, it is further deduced that the stabilization mechanism  
 475 between saccharides and fatty acid molecules may occur in the headgroup region.



476  
 477 Figure 5. PM-IRRAS spectra ( $3000\text{--}2800\text{ cm}^{-1}$ ) of mixed fatty acids at the  
 478 air/seawater interface at different (a) glucose, and (b) trehalose concentrations in the  
 479 subphase.

480 Carboxylic acids possess one hydrogen bond donor (hydroxyl) and one hydrogen  
 481 bond acceptor (carbonyl) within the same functional group, the carboxyl group. The  
 482 carbonyl stretching modes ( $\nu(\text{C}=\text{O})$ ) of the carboxyl group at  $\sim 1734\text{ cm}^{-1}$  (unhydrogen  
 483 bonded),  $1725\text{ cm}^{-1}$  (singly hydrogen bonded) and  $1708\text{ cm}^{-1}$  (doubly hydrogen  
 484 bonded) were observed in seawater (Gericke and Huhnerfuss, 1993), with the strength  
 485 at  $1734\text{ cm}^{-1}$  being the highest (Figure 6). This band component at  $1734\text{ cm}^{-1}$  is put  
 486 down to the conformation with the carbonyl group almost parallel to the water surface  
 487 and the hydroxyl group is oriented toward the water surface, which is not conducive

488 to the formation of hydrogen bond with water subphase (Muro et al., 2010). For  
489 saccharide concentrations ranging from 0.1 to 2 g L<sup>-1</sup>, the unhydrated C=O band was  
490 observed to be depressed, and the singly and doubly hydrogen bonded carbonyl  
491 components at ~1720 and ~1708 cm<sup>-1</sup> became dominant (Johann et al., 2001). At the  
492 highest glucose concentration, the Langmuir model appears to capture a saturation  
493 effect, where the establishment of hydrogen bonds is associated with a strong initial  
494 increase in glucose organic enrichment, followed by surface saturation at higher  
495 organic concentration. We also displayed the wavenumbers, reflectance-absorbance  
496 intensities, peak areas and full width at half maximum (FWHM, cm<sup>-1</sup>) values of each  
497 fitted peak in the region of 1800–1300 cm<sup>-1</sup> in Table S3 in the supplement. The  
498 presence of hydrogen bonds between saccharides and the carbonyls of fatty acids is  
499 well correlated with the observed shifts in the infrared absorption band of carbonyl  
500 groups. Using FTIR experiments, Luzardo et al. (2000) showed that trehalose shifts  
501 the vibrational frequency of the carbonyl group to a lower value, which is an evidence  
502 of the existence of direct hydrogen bonding between trehalose and lipid carbonyl  
503 groups. We believe that saccharides displace water surrounding the fatty acid polar  
504 headgroups and interact strongly with lipid headgroups, resulting in a slight decrease  
505 in hydration near the monolayer interface.



506

507 Figure 6. PM-IRRAS spectra (1800–1300  $\text{cm}^{-1}$ ) of mixed fatty acids at the  
 508 air/seawater interface at different (a) glucose, and (b) trehalose concentrations in the  
 509 subphase.

510 The nonmonotonic hydrogen bond strength shows that the interaction at the  
 511 interface manifests as competing contributions that dominate at different  
 512 concentrations. Within the concentration range studied, saccharides tend to “displace”  
 513 water, creating unique environments. In some recent studies, this “water displacement”  
 514 hypothesis was supported by molecular dynamics (MD) simulations, fluorescence  
 515 microscopy and nuclear magnetic resonance (NMR) (Lambruschini et al., 2000; You  
 516 et al., 2021; Kapla et al., 2015). Previous MD simulation studies showed that the  
 517 hydrogen bond lifetime between trehalose and membrane was longer than that  
 518 established between water and membrane (Villarreal et al., 2004). This is because  
 519 water molecules are more mobile and can exchange more frequently at the interface  
 520 than trehalose. Another study also confirmed that sugar-lipid hydrogen bonds are  
 521 stronger than water-lipid hydrogen bonds due to low endothermicity and they remain  
 522 largely intact even at very high sugar concentrations (You et al., 2021). During SSA  
 523 production, the bubbles remain on the surface for a period of time during which the

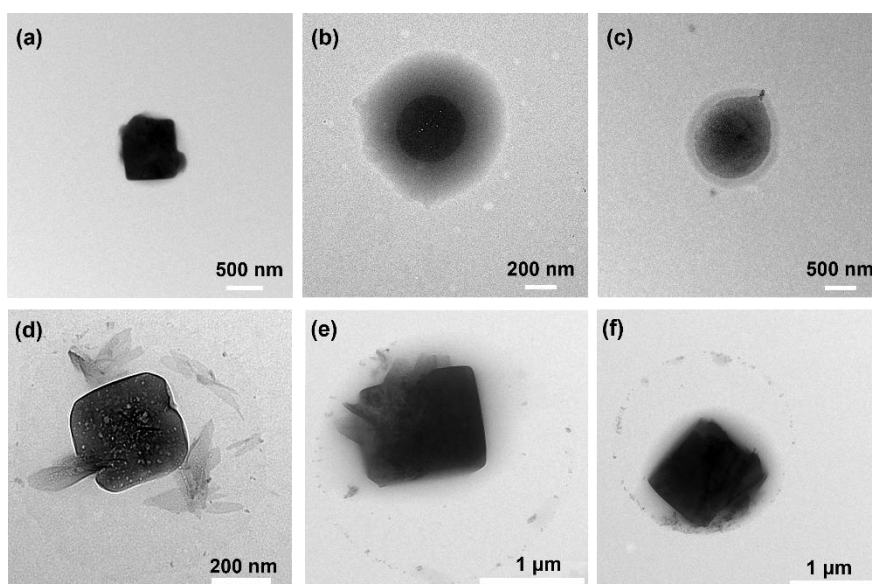
524 bubble's film cap is expelled (Modini et al., 2013), and water and soluble molecules  
525 are removed from the bubble film, a process that is thought to be important for the  
526 high organic matter fraction. These experiments suggest that there are strong  
527 hydrogen bonds between saccharides and fatty acid molecules, so that saccharide  
528 molecules may still be bound to the fatty acid monolayer and not be washed out as the  
529 film cap drains.

530 Long chain fatty acid amphiphiles that spread as a monolayer on the alkaline  
531 subphase undergo dissociation. The ratio of neutral fatty acids and ionized  
532 carboxylates in the monolayer depends on the pH of the subphase solution. At natural  
533 oceanic conditions (pH~8.1), deprotonation of the carboxylic acid groups results in  
534 two carboxylate stretches. The broad and strong antisymmetric carboxylate stretch  
535 ( $\nu_{as}(\text{COO})$ ) were observed at  $\sim 1564 \text{ cm}^{-1}$ , and the symmetric carboxylate stretch  
536 ( $\nu_s(\text{COO})$ ) at  $\sim 1415 \text{ cm}^{-1}$ . The presence of salt in seawater caused the  $\nu_{as}(\text{COO})$  to  
537 split into three peaks at  $\sim 1564$ ,  $\sim 1544$  and  $\sim 1528 \text{ cm}^{-1}$ . Additionally, we found a shift  
538 in the major carboxylate stretching mode from  $1564$  to higher frequency  $\sim 1572 \text{ cm}^{-1}$ ,  
539 which may be indicative of carboxylate dehydration upon interactions with  
540 saccharides. Another distinctive feature in all spectra obtained at  $\sim 1469 \text{ cm}^{-1}$  was  
541 assigned to the  $\text{CH}_2$  scissoring vibration ( $\delta(\text{CH}_2)$ ) of the aliphatic chain (Muro et al.,  
542 2010). This wavenumber value somewhat indicates an orthorhombic subcell structure.  
543 It should be noted that the  $\delta(\text{CH}_2)$  vibrational position for the surface membrane of  
544 the mixed fatty acids reported here is relatively insensitive to saccharides and their  
545 concentrations. This observation confirms the conclusions drawn from the  $\nu_{as}(\text{CH}_2)$

546 and  $\nu_s(\text{CH}_2)$  wavenumbers that higher alkyl chain conformational orders are obtained  
547 either on the surface of pure seawater or on subphases containing glucose or trehalose.

### 548 **3.5 Effect of soluble saccharides on particle morphology**

549 Particle morphology can affect the surface composition, heterogeneous chemistry,  
550 gas-particle partitioning of semi-volatile organics and water uptake of aerosols (Unger  
551 et al., 2020; Ruehl et al., 2016; Lee et al., 2021). We examined the particle  
552 morphology and qualitatively compared SSAs between different model systems,  
553 including the mixed effects of saccharides and fatty acids. Compared to the study by  
554 Unger et al. (2020), the samples we investigated had compositions that were closely  
555 connected to the chemical composition of sea spray aerosols.

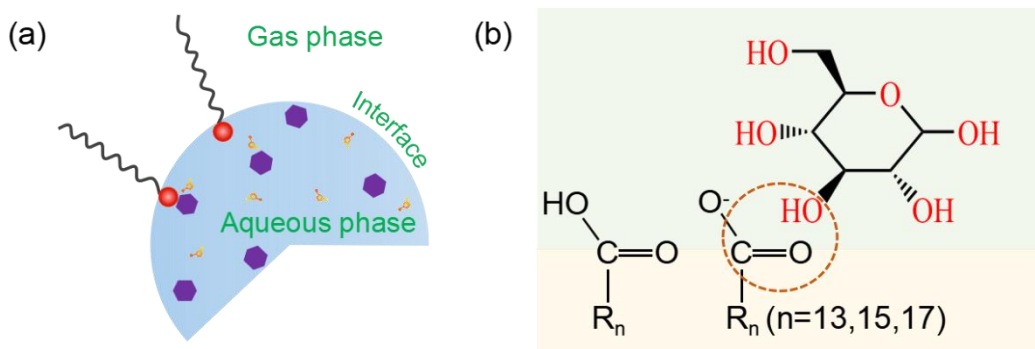


556  
557 Figure 7. TEM images of morphology identified for sea spray aerosols produced from  
558 (a) natural seawater, (b) seawater with glucose and (c) seawater with trehalose without  
559 fatty acids organic layer; (d) natural seawater with fatty acids, (e) seawater with  
560 glucose and fatty acids, (f) seawater with trehalose and fatty acids.

561 Figure 7 depicts TEM images of SSA particles generated by plunging jet sea spray  
562 aerosol generator, which can provide clues about how saccharide and/or fatty acid  
563 components are interacting with sea salt. As can be seen from the Figure 7a, SSA  
564 produced from pure natural seawater by plunging jet exhibited a prism-like  
565 morphology that is predominantly inorganic in nature (Lee et al., 2020). This standard  
566 cubic shape also suggests that NaCl is an important component of natural seawater  
567 sample used in this study. The morphology of SSA particles was strongly affected by  
568 the incorporation of saccharides. In the presence of saccharides, the images indicate  
569 that these SSA particles exhibit a core-shell morphology with the shell portion being  
570 mainly organic in composition, whereas sea salt core are more spherical in nature,  
571 demonstrating that organic substances inhibit the cubic crystallization of NaCl. The  
572 core-shell morphologies adopted here are congruent with previous studies on the  
573 NaCl/Glucose binary system and authentic SSA samples observed using atomic force  
574 microscopy (Ray et al., 2019; Estillore et al., 2017). However, as shown in Figures  
575 7d–f, the presence of fatty acid layer on the surface not only reduces the number  
576 concentration of SSA produced but also tends to maintain the cubic shape of the core  
577 of SSA. When fatty acids and saccharides coexist, we can still observe the  
578 preservation of core-shell structure. In a word, the results presented in this study  
579 suggest that the heterogeneity within a particle type is a function of seawater  
580 chemistry.

### 581 **3.6 Proposed mechanism for bulk saccharide transfer to SSA**

582 The molecular level interactions between small saccharides and fatty acids discussed  
583 in previous sections can be summarized using the model presented in Figure 8.  
584 Aqueous aerosols coated by surface-active organic matter (Figure 8a), such as SSA,  
585 generally hold inverse micelle structures with hydrophilic headgroups pointing toward  
586 the aqueous phase and hydrophobic tails pointing toward the gas phase (Blackshaw et  
587 al., 2019). At the center of the inverse micelle, a water pool is formed that can  
588 dissolve polar substances such as saccharides, proteins, enzymes, amino acids and  
589 nucleic acid. This unique physicochemical environment may enhance the possibility  
590 of saccharides transfer to SSA. Through the Langmuir surface pressure-area  
591 experiment combined with infrared reflection-absorption spectroscopy, we initially  
592 explored the possible mechanism of the transfer of saccharides at the air/water  
593 interface. In a nutshell, we infer that saccharides initially in the aqueous phase move  
594 steadily to the interface and act as a substituent for water molecules, and locate in the  
595 headgroup region of the fatty acids. During the binding process, the saccharides  
596 displace the oriented water molecules that are bound to the fatty acids through  
597 hydrogen bonds, establishing new hydrogen bonds with the carbonyl group of fatty  
598 acids (You et al., 2021).



599

600 Figure 8. (a) Proposed model of fatty acid-saccharide interaction at the air/water  
 601 interface. (b) Description of possible mechanisms of fatty acid-saccharide interaction  
 602 at the air/water interface.

### 603 3.7 Atmospheric implications

604 Despite extensive efforts, the exhaustive relationships between ocean organic carbon  
 605 pools and the chemical composition of SSAs are still outstanding. The coupling of  
 606 this sea spray aerosol simulation generator with the interfacial monolayer model lays  
 607 the foundation for further studies of the material relationship between the ocean and  
 608 SSA. The research reported here yielded two key findings. First, the SSA production  
 609 and particle size distribution are usually extremely sensitive to organic matter, and  
 610 small saccharides dissolved in seawater are critical to the formation, size and  
 611 composition of SSA. Our results strongly support those saccharides can greatly  
 612 promote the generation of SSA particles and make SSA show core-shell morphology  
 613 characteristics. A previous study revealed that the SSA number concentration in  
 614 coastal samples was inversely correlated with salinity, with several organic tracers,  
 615 including dissolved and chromophoric organic carbon (DOC, CDOM), marine  
 616 microgels, and chlorophyll a (Chl-a) being positively correlated, but not associated



617 with viral and bacterial abundances (Park et al., 2019). However, it is more complex  
618 in the real-world environment where the influencing factors are compounded. Other  
619 limitations to this study include the limited representation, by the simple chemical  
620 structural models, of the myriad complex biomolecules that exist in the ocean,  
621 spanning dissolved, colloidal and particulate matter. It is recommended that future  
622 studies targeting the production and property of SSA include the effects of different  
623 types of organic matter to determine whether they fully mimic the arrays of SSA  
624 particles, and include more complete organic matter systems as well as biological  
625 species.

626 Second, it has been suggested that the abundant organic content in SSA plays a key  
627 role in determining the cloud condensation nucleation and ice nucleating activity  
628 (O'dowd et al., 2004). Therefore, climate models demand a predictive representation  
629 of SSA chemical composition to accurately simulate climate processes in the marine  
630 boundary layer (Burrows et al., 2016; Bertram et al., 2018). However, the source of  
631 organic enrichment observed in SSA remains speculative, which poses challenges to  
632 the modeling of the aerosol impact on atmospheric chemistry and climate science. A  
633 recent study has raised that the cooperative adsorption of saccharides with insoluble  
634 lipid monolayers may make important contributions to the sea spray aerosols and even  
635 have climatic consequences with broad research prospects (Burrows et al., 2014).  
636 Their team recently developed a process model for understanding the feedback  
637 relationship between marine biology, sea spray organic matter, and climate, called  
638 OCEANFILMS (Organic Compounds from Ecosystems to Aerosols: Natural Films

639 and Interfaces via Langmuir Molecular Surfactants) sea spray organic aerosol  
640 emissions – implementation in a global climate model and impacts on clouds  
641 (Burrows et al., 2022). In this work, we used the Langmuir monolayer to model  
642 possible interactions between subphase soluble saccharides and surface fatty acid  
643 molecules. A subsequent study used infrared reflection-absorption spectroscopy to  
644 determine the interaction mechanism between two simple soluble saccharides and  
645 tightly packed fatty acids monolayers at the air/water interface. Combining the above  
646 experimental results, we infer that the hydrogen bonding interaction between  
647 saccharides and the carbonyl group of surface insoluble fatty acid molecules  
648 contributes to its transfer from the ocean to the atmosphere. At present, this  
649 mechanism of saccharides transfer and enrichment has not been emphasized in the  
650 model describing SSA formation. Furthermore, our results may be an effective  
651 complement and development to OCEANFILMS model theory, and by adding the  
652 chemical interaction between soluble saccharides and an insoluble fatty acid  
653 surfactant monolayer, the consistency of modeled sea spray chemistry with observed  
654 marine aerosol chemistry may be improved. To further examine the feasibility of the  
655 hydrogen bonding mechanism as an interfacial organic enrichment mechanism, it is  
656 necessary to further explore and verify the interaction of other carbohydrates with  
657 common surface-insoluble molecules in future studies.

#### 658 **4 Conclusions**

659 In summary, we simulated the production of SSA in natural seawater spiked with two

660 common soluble saccharides using a plunging water jet generator and revealed the  
661 possible mechanism of saccharide transfer from bulk seawater into SSA combined  
662 with surface sensitive infrared spectroscopy techniques. We confirmed that glucose  
663 and trehalose can significantly promote the production of SSA and alter the surface  
664 morphology of SSA particles. This highlights the potential for a direct oceanic source  
665 of carbohydrate organics through bubble bursting. In addition, trehalose showed  
666 stronger promoting ability than glucose, while the surface fatty acid layer played an  
667 inhibitory role. Using the mixture of saturated fatty acids MA, PA and SA as the proxy  
668 of SSA surface film, the  $\pi$ -A isotherms provided strong evidence that saccharides can  
669 interact with insoluble fatty acid monolayers and be adsorbed at the monolayer, which  
670 caused expansion of the monolayer and made the films heterogeneous. According to  
671 the IRRAS spectra, soluble saccharides did not produce a significant impact on the  
672 order of fatty acid alkyl chains. We further infer that soluble saccharides are mainly  
673 located on the subsurface below the monolayer, and interact with carbonyl groups of  
674 fatty acids by forming hydrogen bonds to facilitate their sea-air transfer. Crucially,  
675 this work provides physical and molecular signatures of potentially important  
676 saccharides transfer mechanism with general implications for understanding how  
677 saccharide-lipid interactions affect sea spray aerosol systems for real-world.

#### 678 **Data availability**

679 Data are available by contacting the corresponding author.

680 **Supplement**

681 The supplement related to this article is available online at:

682 **Author contributions**

683 MX: conceived the experiment, data curation, formal analysis, writing original draft,  
684 writing-review & editing. NTT: writing - review & editing. JL: writing - review &  
685 editing. LD: supervision, conceived the experiment, funding acquisition, writing -  
686 review & editing.

687 **Competing interests**

688 The author declare that they have no conflict of interest.

689 **Financial support**

690 The authors acknowledge support from National Natural Science Foundation of China  
691 (22076099, 21876098), Youth Innovation Program of Universities in Shandong  
692 Province (2019KJD007), and Fundamental Research Fund of Shandong University  
693 (2020QNQT012).

694

695 **References**

- 696 Bertram, T. H., Cochran, R. E., Grassian, V. H., and Stone, E. A.: Sea spray aerosol  
697 chemical composition: Elemental and molecular mimics for laboratory studies of  
698 heterogeneous and multiphase reactions, *Chem. Soc. Rev.*, 47, 2374-2400,  
699 10.1039/c7cs00008a, 2018.
- 700 Blackshaw, K. J., Varnecky, M. G., and Patterson, J. D.: Interfacial structure and  
701 partitioning of nitrate ions in reverse micelles, *J. Phys. Chem. A*, 123, 336-342,  
702 10.1021/acs.jpca.8b09751, 2019.
- 703 Brooks, S. D. and Thornton, D. C. O.: Marine aerosols and clouds, *Annu. Rev. Mar.*  
704 *Sci.*, 10, 289-313, 10.1146/annurev-marine-121916-063148, 2018.
- 705 Burrows, S. M., Ogunro, O., Frossard, A. A., Russell, L. M., Rasch, P. J., and Elliott,  
706 S. M.: A physically based framework for modeling the organic fractionation of sea  
707 spray aerosol from bubble film Langmuir equilibria, *Atmos. Chem. Phys.*, 14,  
708 13601-13629, 10.5194/acp-14-13601-2014, 2014.
- 709 Burrows, S. M., Gobrogge, E., Fu, L., Link, K., Elliott, S. M., Wang, H. F., and  
710 Walker, R.: OCEANFILMS-2: Representing coadsorption of saccharides in marine  
711 films and potential impacts on modeled marine aerosol chemistry, *Geophys. Res. Lett.*,  
712 43, 8306-8313, 10.1002/2016gl069070, 2016.
- 713 Burrows, S. M., Easter, R. C., Liu, X. H., Ma, P. L., Wang, H. L., Elliott, S. M., Singh,  
714 B., Zhang, K., and Rasch, P. J.: OCEANFILMS (Organic Compounds from  
715 Ecosystems to Aerosols: Natural Films and Interfaces via Langmuir Molecular  
716 Surfactants) sea spray organic aerosol emissions - implementation in a global climate  
717 model and impacts on clouds, *Atmos. Chem. Phys.*, 22, 5223-5251,  
718 10.5194/acp-22-5223-2022, 2022.
- 719 Carter-Fenk, K. A. and Allen, H. C.: Collapse mechanisms of nascent and aged sea  
720 spray aerosol proxy films, *Atmosphere*, 9, 503, ARTN 503  
721 10.3390/atmos9120503, 2018.
- 722 Christiansen, S., Salter, M. E., Gorokhova, E., Nguyen, Q. T., and Bilde, M.: Sea  
723 spray aerosol formation: Laboratory results on the role of air entrainment, water  
724 temperature and phytoplankton biomass, *Environ. Sci. Technol.*, 53, 13107-13116,  
725 10.1021/acs.est.9b04078, 2019.
- 726 Clark, G. A., Henderson, J. M., Heffern, C., Akgun, B., Majewski, J., and Lee, K. Y.  
727 C.: Synergistic interactions of sugars/polyols and monovalent salts with phospholipids  
728 depend upon sugar/polyol complexity and anion identity, *Langmuir*, 31, 12688-12698,  
729 10.1021/acs.langmuir.5b02815, 2015.
- 730 Cochran, R. E., Laskina, O., Jayarathne, T., Laskin, A., Laskin, J., Lin, P., Sultana, C.,  
731 Lee, C., Moore, K. A., Cappa, C. D., Bertram, T. H., Prather, K. A., Grassian, V. H.,  
732 and Stone, E. A.: Analysis of organic anionic surfactants in fine and coarse fractions  
733 of freshly emitted sea spray aerosol, *Environ. Sci. Technol.*, 50, 2477-2486,  
734 10.1021/acs.est.5b04053, 2016.
- 735 Cochran, R. E., Laskina, O., Trueblood, J. V., Estillore, A. D., Morris, H. S.,  
736 Jayarathne, T., Sultana, C. M., Lee, C., Lin, P., Laskin, J., Laskin, A., Dowling, J. A.,

737 Qin, Z., Cappa, C. D., Bertram, T. H., Tivanski, A. V., Stone, E. A., Prather, K. A., and  
738 Grassian, V. H.: Molecular diversity of sea spray aerosol particles: Impact of ocean  
739 biology on particle composition and hygroscopicity, *Chem*, 2, 655-667,  
740 10.1016/j.chempr.2017.03.007, 2017.

741 Cravigan, L. T., Mallet, M. D., Vaattovaara, P., Harvey, M. J., Law, C. S., Modini, R.  
742 L., Russell, L. M., Stelcer, E., Cohen, D. D., Olsen, G., Safi, K., Burrell, T. J., and  
743 Ristovski, Z.: Sea spray aerosol organic enrichment, water uptake and surface tension  
744 effects, *Atmos. Chem. Phys.*, 20, 7955-7977, 10.5194/acp-20-7955-2020, 2020.

745 Crowe, J. H., Whittam, M. A., Chapman, D., and Crowe, L. M.: Interactions of  
746 phospholipid monolayers with carbohydrates, *Biochim Biophys Acta*, 769, 151-159,  
747 10.1016/0005-2736(84)90018-x, 1984.

748 Cunliffe, M., Engel, A., Frka, S., Gašparović, B., Guitart, C., Murrell, J. C., Salter, M.,  
749 Stolle, C., Upstill-Goddard, R., and Wurl, O.: Sea surface microlayers: A unified  
750 physicochemical and biological perspective of the air–ocean interface, *Prog.*  
751 *Oceanogr.*, 109, 104-116, 10.1016/j.pocean.2012.08.004, 2013.

752 de Vasquez, M. G. V., Rogers, M. M., Carter-Fenk, K. A., and Allen, H. C.:  
753 Discerning poly- and monosaccharide enrichment mechanisms: Alginate and  
754 glucuronate adsorption to a stearic acid sea surface microlayer, *ACS Earth Space*  
755 *Chem.*, 6, 1581-1595, 10.1021/acsearthspacechem.2c00066, 2022.

756 Deane, G. B. and Stokes, M. D.: Scale dependence of bubble creation mechanisms in  
757 breaking waves, *Nature*, 418, 839-844, 10.1038/nature00967, 2002.

758 Elliott, S., Burrows, S. M., Deal, C., Liu, X., Long, M., Ogunro, O., Russell, L. M.,  
759 and Wingenter, O.: Prospects for simulating macromolecular surfactant chemistry at  
760 the ocean-atmosphere boundary, *Environ. Res. Lett.*, 9, 064012,  
761 10.1088/1748-9326/9/6/064012, 2014.

762 Estillore, A. D., Morris, H. S., Or, V. W., Lee, H. D., Alves, M. R., Marciano, M. A.,  
763 Laskina, O., Qin, Z., Tivanski, A. V., and Grassian, V. H.: Linking hygroscopicity and  
764 the surface microstructure of model inorganic salts, simple and complex  
765 carbohydrates, and authentic sea spray aerosol particles, *Phys. Chem. Chem. Phys.*, 19,  
766 21101-21111, 10.1039/c7cp04051b, 2017.

767 Facchini, M. C., Rinaldi, M., Decesari, S., Carbone, C., Finessi, E., Mircea, M., Fuzzi,  
768 S., Ceburnis, D., Flanagan, R., Nilsson, E. D., de Leeuw, G., Martino, M., Woeltjen, J.,  
769 and O'Dowd, C. D.: Primary submicron marine aerosol dominated by insoluble  
770 organic colloids and aggregates, *Geophys. Res. Lett.*, 35, L17814,  
771 10.1029/2008gl034210, 2008.

772 Frossard, A. A., Russell, L. M., Burrows, S. M., Elliott, S. M., Bates, T. S., and Quinn,  
773 P. K.: Sources and composition of submicron organic mass in marine aerosol particles,  
774 *J. Geophys. Res.-Atmos.*, 119, 12977-13003, 10.1002/2014jd021913, 2014.

775 Fuentes, E., Coe, H., Green, D., de Leeuw, G., and McFiggans, G.:  
776 Laboratory-generated primary marine aerosol via bubble-bursting and atomization,  
777 *Atmos. Meas. Tech.*, 3, 141-162, 10.5194/amt-3-141-2010, 2010.

778 Gericke, A. and Huhnerfuss, H.: In-situ investigation of saturated long-chain  
779 fatty-acids at the air-water interface by external Infrared reflection-absorption  
780 spectrometry, *J. Phys. Chem.*, 97, 12899-12908, 10.1021/j100151a044, 1993.

781 Hasenecz, E. S., Kaluarachchi, C. P., Lee, H. D., Tivanski, A. V., and Stone, E. A.:  
782 Saccharide transfer to sea spray aerosol enhanced by surface activity, calcium, and  
783 protein interactions, *ACS Earth Space Chem.*, 3, 2539-2548,  
784 10.1021/acsearthspacechem.9b00197, 2019.

785 Hasenecz, E. S., Jayarathne, T., Pendergraft, M. A., Santander, M. V., Mayer, K. J.,  
786 Sauer, J., Lee, C., Gibson, W. S., Kruse, S. M., Malfatti, F., Prather, K. A., and Stone,  
787 E. A.: Marine bacteria affect saccharide enrichment in sea spray aerosol during a  
788 phytoplankton bloom, *ACS Earth Space Chem.*, 4, 1638-1649,  
789 10.1021/acsearthspacechem.0c00167, 2020.

790 Hawkins, L. N. and Russell, L.: Polysaccharides, proteins, and phytoplankton  
791 fragments: Four chemically distinct types of marine primary organic aerosol classified  
792 by single particle spectromicroscopy, *Adv. Meteorol.*, 2010, 612132,  
793 10.1155/2010/612132, 2010.

794 Hultin, K. A. H., Nilsson, E. D., Krejci, R., Martensson, E. M., Ehn, M., Hagstrom, A.,  
795 and de Leeuw, G.: In situ laboratory sea spray production during the Marine Aerosol  
796 Production 2006 cruise on the northeastern Atlantic Ocean, *J. Geophys. Res.-Atmos.*,  
797 115, D06201, 10.1029/2009jd012522, 2010.

798 Johann, R., Vollhardt, D., and Mohwald, H.: Study of the pH dependence of head  
799 group bonding in arachidic acid monolayers by polarization modulation infrared  
800 reflection absorption spectroscopy, *Colloid Surf. A-Physicochem. Eng. Asp.*, 182,  
801 311-320, 10.1016/s0927-7757(00)00812-8, 2001.

802 Kapla, J., Engstrom, O., Stevansson, B., Wohler, J., Widmalm, G., and Maliniak, A.:  
803 Molecular dynamics simulations and NMR spectroscopy studies of trehalose-lipid  
804 bilayer systems, *Phys. Chem. Chem. Phys.*, 17, 22438-22447, 10.1039/c5cp02472b,  
805 2015.

806 King, S. M., Butcher, A. C., Rosenoern, T., Coz, E., Lieke, K. I., de Leeuw, G.,  
807 Nilsson, E. D., and Bilde, M.: Investigating primary marine aerosol properties: CCN  
808 activity of sea salt and mixed inorganic-organic particles, *Environ. Sci. Technol.*, 46,  
809 10405-10412, 10.1021/es300574u, 2012.

810 Lambruschini, C., Relini, A., Ridi, A., Cordone, L., and Gliozzi, A.: Trehalose  
811 interacts with phospholipid polar heads in Langmuir monolayers, *Langmuir*, 16,  
812 5467-5470, 10.1021/la991641e, 2000.

813 Lee, C., Dommer, A. C., Schiffer, J. M., Amaro, R. E., Grassian, V. H., and Prather, K.  
814 A.: Cation-driven lipopolysaccharide morphological changes impact heterogeneous  
815 reactions of nitric acid with sea spray aerosol particles, *J. Phys. Chem. Lett.*, 12,  
816 5023-5029, 10.1021/acs.jpcclett.1c00810, 2021.

817 Lee, H. D., Wigley, S., Lee, C., Or, V. W., Hasenecz, E. S., Stone, E. A., Grassian, V.  
818 H., Prather, K. A., and Tivanski, A. V.: Physicochemical mixing state of sea spray  
819 aerosols: Morphologies exhibit size dependence, *ACS Earth Space Chem.*, 4,  
820 1604-1611, 10.1021/acsearthspacechem.0c00153, 2020.

821 Lee, K. Y. C.: Collapse mechanisms of Langmuir monolayers, *Annu. Rev. Phys.*  
822 *Chem.*, 59, 771-791, 10.1146/annurev.physchem.58.032806.104619, 2008.

823 Li, S. Y., Jiang, X. T., Roveretto, M., George, C., Liu, L., Jiang, W., Zhang, Q. Z.,  
824 Wang, W. X., Ge, M. F., and Du, L.: Photochemical aging of atmospherically reactive

825 organic compounds involving brown carbon at the air-aqueous interface, *Atmos.*  
826 *Chem. Phys.*, 19, 9887-9902, 10.5194/acp-19-9887-2019, 2019.

827 Link, K. A., Spurzem, G. N., Tuladhar, A., Chase, Z., Wang, Z. M., Wang, H. F., and  
828 Walker, R. A.: Cooperative adsorption of trehalose to DPPC monolayers at the  
829 water-air interface studied with vibrational sum frequency generation, *J. Phys. Chem.*  
830 *B*, 123, 8931-8938, 10.1021/acs.jpcc.9b07770, 2019a.

831 Link, K. A., Spurzem, G. N., Tuladhar, A., Chase, Z., Wang, Z. M., Wang, H. F., and  
832 Walker, R. A.: Organic enrichment at aqueous interfaces: Cooperative adsorption of  
833 glucuronic acid to DPPC monolayers studied with vibrational sum frequency  
834 generation, *J. Phys. Chem. A*, 123, 5621-5632, 10.1021/acs.jpca.9b02255, 2019b.

835 Liu, L. R., Du, L., Xu, L., Li, J. L., and Tsona, N. T.: Molecular size of surfactants  
836 affects their degree of enrichment in the sea spray aerosol formation, *Environ. Res.*,  
837 206, 112555, 10.1016/j.envres.2021.112555, 2022.

838 Luzardo, M. D., Amalfa, F., Nunez, A. M., Diaz, S., de Lopez, A. C. B., and Disalvo,  
839 E. A.: Effect of trehalose and sucrose on the hydration and dipole potential of lipid  
840 bilayers, *Biophys. J.*, 78, 2452-2458, 10.1016/s0006-3495(00)76789-0, 2000.

841 Lv, C., Tsona, N. T., and Du, L.: Sea spray aerosol formation: Results on the role of  
842 different parameters and organic concentrations from bubble bursting experiments,  
843 *Chemosphere*, 252, 126456, 10.1016/j.chemosphere.2020.126456, 2020.

844 Modini, R. L., Russell, L. M., Deane, G. B., and Stokes, M. D.: Effect of soluble  
845 surfactant on bubble persistence and bubble-produced aerosol particles, *J. Geophys.*  
846 *Res.-Atmos.*, 118, 1388-1400, 10.1002/jgrd.50186, 2013.

847 Muro, M., Itoh, Y., and Hasegawa, T.: A conformation and orientation model of the  
848 carboxylic group of fatty acids dependent on chain length in a Langmuir monolayer  
849 film studied by polarization-modulation infrared reflection absorption spectroscopy, *J.*  
850 *Phys. Chem. B*, 114, 11496-11501, 10.1021/jp105862q, 2010.

851 O'Dowd, C. D., Facchini, M. C., Cavalli, F., Ceburnis, D., Mircea, M., Decesari, S.,  
852 Fuzzi, S., Yoon, Y. J., and Putaud, J. P.: Biogenically driven organic contribution to  
853 marine aerosol, *Nature*, 431, 676-680, 10.1038/nature02959, 2004.

854 Pakulski, J. D. and Benner, R.: An improved method for the hydrolysis and MBTH  
855 analysis of dissolved and particulate carbohydrates in seawater, *Mar. Chem.*, 40,  
856 143-160, 10.1016/0304-4203(92)90020-B, 1992.

857 Park, J., Dall'Osto, M., Park, K., Kim, J. H., Park, J., Park, K. T., Hwang, C. Y., Jang,  
858 G. I., Gim, Y., Kang, S., Park, S., Jin, Y. K., Yum, S. S., Simo, R., and Yoon, Y. J.:  
859 Arctic primary aerosol production strongly influenced by riverine organic matter,  
860 *Environ. Sci. Technol.*, 53, 8621-8630, 10.1021/acs.est.9b03399, 2019.

861 Partanen, A. I., Dunne, E. M., Bergman, T., Laakso, A., Kokkola, H., Ovadnevaite, J.,  
862 Sogacheva, L., Baisnee, D., Sciare, J., Manders, A., O'Dowd, C., de Leeuw, G., and  
863 Korhonen, H.: Global modelling of direct and indirect effects of sea spray aerosol  
864 using a source function encapsulating wave state, *Atmos. Chem. Phys.*, 14,  
865 11731-11752, 10.5194/acp-14-11731-2014, 2014.

866 Pavinatto, F. J., Caseli, L., Pavinatto, A., dos Santos, D. S., Nobre, T. M., Zaniquelli,  
867 M. E. D., Silva, H. S., Miranda, P. B., and de Oliveira, O. N.: Probing chitosan and  
868 phospholipid interactions using Langmuir and Langmuir-Blodgett films as cell



869 membrane models, *Langmuir*, 23, 7666-7671, 10.1021/la700856a, 2007.

870 Perkins, R. and Vaida, V.: Phenylalanine increases membrane permeability, *J. Am.*  
871 *Chem. Soc.*, 139, 14388-14391, 10.1021/jacs.7b09219, 2017.

872 Prather, K. A., Bertram, T. H., Grassian, V. H., Deane, G. B., Stokes, M. D., DeMott, P.  
873 J., Aluwihare, L. I., Palenik, B. P., Azam, F., Seinfeld, J. H., Moffet, R. C., Molina, M.  
874 J., Cappa, C. D., Geiger, F. M., Roberts, G. C., Russell, L. M., Ault, A. P., Baltrusaitis,  
875 J., Collins, D. B., Corrigan, C. E., Cuadra-Rodriguez, L. A., Ebben, C. J., Forestieri, S.  
876 D., Guasco, T. L., Hersey, S. P., Kim, M. J., Lambert, W. F., Modini, R. L., Mui, W.,  
877 Pedler, B. E., Ruppel, M. J., Ryder, O. S., Schoepp, N. G., Sullivan, R. C., and Zhao,  
878 D. F.: Bringing the ocean into the laboratory to probe the chemical complexity of sea  
879 spray aerosol, *Proc. Natl. Acad. Sci. U. S. A.*, 110, 7550-7555,  
880 10.1073/pnas.1300262110, 2013.

881 Quinn, P. K., Coffman, D. J., Johnson, J. E., Upchurch, L. M., and Bates, T. S.: Small  
882 fraction of marine cloud condensation nuclei made up of sea spray aerosol, *Nat.*  
883 *Geosci.*, 10, 674-679, 10.1038/ngeo3003, 2017.

884 Quinn, P. K., Collins, D. B., Grassian, V. H., Prather, K. A., and Bates, T. S.:  
885 Chemistry and related properties of freshly emitted sea spray aerosol, *Chem. Rev.*,  
886 115, 4383-4399, 10.1021/cr500713g, 2015.

887 Quinn, P. K., Bates, T. S., Schulz, K. S., Coffman, D. J., Frossard, A. A., Russell, L.  
888 M., Keene, W. C., and Kieber, D. J.: Contribution of sea surface carbon pool to  
889 organic matter enrichment in sea spray aerosol, *Nat. Geosci.*, 7, 228-232,  
890 10.1038/ngeo2092, 2014.

891 Ray, K. K., Lee, H. D., Gutierrez, M. A., Chang, F. J., and Tivanski, A. V.: Correlating  
892 3D morphology, phase state, and viscoelastic properties of individual  
893 substrate-deposited particles, *Anal. Chem.*, 91, 7621-7630,  
894 10.1021/acs.analchem.9b00333, 2019.

895 Ruehl, C. R., Davies, J. F., and Wilson, K. R.: An interfacial mechanism for cloud  
896 droplet formation on organic aerosols, *Science*, 351, 1447-1450,  
897 10.1126/science.aad4889, 2016.

898 Russell, L. M., Hawkins, L. N., Frossard, A. A., Quinn, P. K., and Bates, T. S.:  
899 Carbohydrate-like composition of submicron atmospheric particles and their  
900 production from ocean bubble bursting, *Proc. Natl. Acad. Sci. U. S. A.*, 107,  
901 6652-6657, 10.1073/pnas.0908905107, 2010.

902 Schill, S., Burrows, S., Hasenecz, E., Stone, E., and Bertram, T.: The impact of  
903 divalent cations on the enrichment of soluble saccharides in primary sea spray aerosol,  
904 *Atmosphere*, 9, 476, 10.3390/atmos9120476, 2018.

905 Schmitt-Kopplin, P., Liger-Belair, G., Koch, B. P., Flerus, R., Kattner, G., Harir, M.,  
906 Kanawati, B., Lucio, M., Tziotis, D., Hertkorn, N., and Gebefugi, I.: Dissolved  
907 organic matter in sea spray: a transfer study from marine surface water to aerosols,  
908 *Biogeosciences*, 9, 1571-1582, 10.5194/bg-9-1571-2012, 2012.

909 Unger, I., Saak, C. M., Salter, M., Zieger, P., Patanen, M., and Bjorneholm, O.:  
910 Influence of organic acids on the surface composition of sea spray aerosol, *J. Phys.*  
911 *Chem. A*, 124, 422-429, 10.1021/acs.jpca.9b09710, 2020.

912 van Pinxteren, M., Muller, C., Iinuma, Y., Stolle, C., and Herrmann, H.: Chemical

913 characterization of dissolved organic compounds from coastal sea surface micro  
914 layers (Baltic Sea, Germany), *Environ. Sci. Technol.*, 46, 10455-10462,  
915 10.1021/es204492b, 2012.

916 van Pinxteren, M., Fomba, K. W., Triesch, N., Stolle, C., Wurl, O., Bahlmann, E.,  
917 Gong, X. D., Voigtlander, J., Wex, H., Robinson, T. B., Barthel, S., Zeppenfeld, S.,  
918 Hoffmann, E. H., Roveretto, M., Li, C. L., Grosselin, B., Daele, V., Senf, F., van  
919 Pinxteren, D., Manzi, M., Zabalegui, N., Frka, S., Gasparovic, B., Pereira, R., Li, T.,  
920 Wen, L., Li, J. R., Zhu, C., Chen, H., Chen, J. M., Fiedler, B., Von Tumpling, W.,  
921 Read, K. A., Punjabi, S., Lewis, A. C., Hopkins, J. R., Carpenter, L. J., Peeken, I.,  
922 Rixen, T., Schulz-Bull, D., Monge, M. E., Mellouki, A., George, C., Stratmann, F.,  
923 and Herrmann, H.: Marine organic matter in the remote environment of the Cape  
924 Verde islands - an introduction and overview to the MarParCloud campaign, *Atmos.*  
925 *Chem. Phys.*, 20, 6921-6951, 10.5194/acp-20-6921-2020, 2020.

926 Villarreal, M. A., Diaz, S. B., Disalvo, E. A., and Montich, G. G.: Molecular dynamics  
927 simulation study of the interaction of trehalose with lipid membranes, *Langmuir*, 20,  
928 7844-7851, 10.1021/la049485l, 2004.

929 Wang, X. F., Deane, G. B., Moore, K. A., Ryder, O. S., Stokes, M. D., Beall, C. M.,  
930 Collins, D. B., Santander, M. V., Burrows, S. M., Sultana, C. M., and Prather, K. A.:  
931 The role of jet and film drops in controlling the mixing state of submicron sea spray  
932 aerosol particles, *Proc. Natl. Acad. Sci. U. S. A.*, 114, 6978-6983,  
933 10.1073/pnas.1702420114, 2017.

934 Wurl, O., Ekau, W., Landing, W. M., and Zappa, C. J.: Sea surface microlayer in a  
935 changing ocean - A perspective, *Elementa. Sci. Anthropol.*, 5, 31, 10.1525/elementa.228,  
936 2017.

937 Xu, M. L., Tsona, N. T., Cheng, S. M., Li, J. L., and Du, L.: Unraveling interfacial  
938 properties of organic-coated marine aerosol with lipase incorporation, *Sci. Total*  
939 *Environ.*, 782, 146893, 10.1016/j.scitotenv.2021.146893, 2021.

940 Xu, W., Ovadnevaite, J., Fossum, K. N., Lin, C. S., Huang, R. J., Ceburnis, D., and  
941 O'Dowd, C.: Sea spray as an obscured source for marine cloud nuclei, *Nat. Geosci.*,  
942 15, 282-286, 10.1038/s41561-022-00917-2, 2022.

943 You, X., Lee, E., Xu, C., and Baiz, C. R.: Molecular mechanism of cell membrane  
944 protection by sugars: A study of interfacial H-Bond networks, *J. Phys. Chem. Lett.*, 12,  
945 9602-9607, 10.1021/acs.jpcclett.1c02451, 2021.

946 Zeppenfeld, S., van Pinxteren, M., van Pinxteren, D., Wex, H., Berdalet, E., Vaque, D.,  
947 Dall'Osto, M., and Herrmann, H.: Aerosol marine primary carbohydrates and  
948 atmospheric transformation in the Western Antarctic Peninsula, *ACS Earth Space*  
949 *Chem.*, 5, 1032-1047, 10.1021/acsearthspacechem.0c00351, 2021.

950